

Topological split-ring resonator based metamaterials with \mathcal{PT} symmetry relying on gain and loss

N. Lazarides^{1,2}, G. P. Tsironis^{1,2}

¹*Institute of Theoretical and Computational Physics & Department of Physics, University of Crete, Herakleio, Greece*

²*National University of Science and Technology “MISiS”, Leninsky Prospekt 4, Moscow, 119049, Russia*

(Dated: August 5, 2020)

A one-dimensional metamaterial with parity-time (\mathcal{PT}) symmetry that relies on balanced gain and loss is introduced, comprising of magnetically coupled split-ring resonators (SRRs). A particular topology that combines a non-trivial (topological) dimer configuration with a trivial (non-topological) dimer configuration which are separated by a central SRR with neither gain or loss, is investigated. By focusing on the dynamical aspects of such a topological \mathcal{PT} metamaterial (PTMM), the existence of *topologically protected interface states* which are localized at the central SRR is demonstrated numerically. The solution of the corresponding *quadratic eigenvalue problem* reveals that the protected state is actually a robust eigenmode of the topological PTMM, whose eigenvalue is isolated in the middle of the gap (mid-gap state) of the two-band frequency spectrum. Direct numerical simulations have been further used to determine the robustness and dynamic stability of these states in the parameter space of the *dimerization strength* and the *gain-loss coefficient*.

PACS numbers: 63.20.Pw, 11.30.Er, 41.20.-q, 78.67.Pt

I. INTRODUCTION

The application of topology, the mathematical theory of conserved properties under continuous deformations, is creating new opportunities for several fields including photonics^{1–3}, acoustics^{4–6}, and mechanics^{6–9}. This field was inspired by the discovery of *topological insulators*^{6,10–12}, in which interfacial electrons transport without dissipation, even in the presence of impurities. Similarly, using carefully designed topologies allows the creation of interfaces that support new protected states in photonics^{13,14} and elastic photonic crystals¹⁵.

Recently, the topological properties of photonic \mathcal{PT} -symmetric crystals¹³ and other non-Hermitian systems^{16–23} have attracted a lot of interest. Moreover, the topological insulating properties^{24,25} and the topological transitions^{26,27} of various metamaterials have been investigated. Further, topological mechanical metamaterials²⁸ and topological metamaterials based on polariton rings²⁹ were introduced. These and similar concepts were recently transferred into electronic and electrical circuit devices^{30,31} and also in split-ring resonator (SRR) chains^{32,33}, where robust topologically protected states were detected.

Here, a one-dimensional (1D) parity-time (\mathcal{PT}) symmetric metamaterial (PTMM) comprising SRRs which are magnetically coupled through dipole-dipole interactions due to their mutual inductance^{34–37}, is considered. The exact configuration (Fig. 1) combines a topological with a non-topological dimer chain of SRRs, both having alternating gain and loss. The chains are separated by a central SRR with neither gain or loss¹³. Note that non-topological PTMMs support localized states either due to nonlinearity^{35,36} or due to a flat band in their spectrum³⁷. Symmetry-protected localized states whose localization lengths are robust against gain and loss have been investigated in \mathcal{PT} -symmetric ladder

lattices³⁸, passive \mathcal{PT} -symmetric microwave resonator Su-Schrieffer-Heeger (SSH) chains³⁹, complex photonic lattices with spatially distributed gain and loss¹⁴, SSH chains with a pair of \mathcal{PT} -symmetric defects⁴⁰, non-Hermitian trimerized optical lattices⁴¹, and complex SSH lattice models containing gain and loss on alternating sites¹⁸.

The present work focuses on the dynamical aspects of the topological PTMM in Fig. 1, and in particular on the topological protection of localized interface states in the parameter space of the gain-loss coefficient γ and the dimerization strength $\delta\lambda_M = |\lambda_M - \lambda'_M|$, with λ_M (λ'_M) being the intra-dimer (inter-dimer) magnetic coupling strength between neighboring SRRs separated by center-to-center distance d (d'). Although the coupling between SRRs is generally both electric and magnetic, the former can be much weaker than the latter under certain conditions. Here, the electric coupling is neglected for simplicity; however, qualitatively similar results are obtained if both couplings are taken into account.



FIG. 1: (color online) Schematic of the topological \mathcal{PT} -metamaterial. The blue, red, and green split-ring resonator(s) have loss, gain, and neither gain nor loss, respectively. SRRs separated by center-to-center distance d (d') are coupled magnetically and electrically through intra-dimer (inter-dimer) coefficients λ_M and λ_E (λ'_M and λ'_E), respectively.

In the next Section, the dynamic equations for the topological PTMM are presented in matrix form, along with a general description of the equivalent circuit model. In Section III, those equations are simulated with single-site initial excitations, to demonstrate the emergence of topologically protected localized interface states. The corresponding quadratic eigenvalue problem is solved in

Section IV, revealing that the protected states are robust eigenmodes with an isolated midgap eigenvalue. Conclusions are given in Section V.

II. MODEL DYNAMICAL EQUATIONS

Consider the topological PTMM of Fig. 1, in which the SRRs have either loss (blue), or gain (red), or neither of those (green). Their total number is $N = 5 + 4m$, where m positive integer or zero. In the equivalent circuit model picture, the SRRs are regarded as resistive-inductive-capacitive (RLC) circuits, featuring resistance R , inductance L , and capacitance C . Note that the resistance is positive, $+R$ (negative, $-R$) for the SRRs with loss (gain), while it is zero for the central SRR. The SRRs are considered to be coupled magnetically to their nearest neighbors through their mutual inductance M and M' for separating center-to-center distance d and d' , respectively ($d < d'$). The intra-dimer (inter-dimer) coupling coefficients, defined as $\lambda_M = M/L$ ($\lambda'_M = M'/L$), usually assume rather low values that justify the nearest-neighbor coupling approximation. An initial excitation induces currents in the SRRs which either decay or amplify depending on them having respectively loss or gain. However, the balance of gain and loss can lead the system in a steady state in which periodic solutions exist as long as the gain-loss coefficient γ remains below its critical value γ_c that separates the exact from the broken \mathcal{PT} phase.

The dynamics of the topological PTMM is determined by the evolution of the charges Q_n ($n = 1, 2, 3, \dots, N$) accumulated at the banks of the capacitors C of the SRRs. In order to exemplify the model, let us consider the SRR at $n = n_e - 1$ (i.e., the left nearest neighbor of the central SRR in Fig. 1), whose dynamic equation can be derived from Kirchhoff's voltage law and the relation $I_{n_e-1} = dQ_{n_e-1}/dt$, as

$$\frac{d^2}{dt^2} (MQ_{n_e-2} + LQ_{n_e-1} + M'Q_{n_e}) - R \frac{dQ_{n_e-1}}{dt} + \frac{Q_{n_e-1}}{C} = 0,$$

where I_{n_e-1} is the current in the SRR at $n = n_e - 1$. That equation can be casted in the dimensionless form

$$\frac{d^2}{d\tau^2} (\lambda_M q_{n_e-2} + q_{n_e-1} + \lambda'_M q_{n_e}) - \gamma \frac{dq_{n_e-1}}{d\tau} + q_{n_e-1} = 0,$$

using the relations $\tau = \omega_{LC} t$ and $q_{n_e-1} = Q_{n_e-1}/(CU_0)$, where U_0 is a characteristic voltage across the slits of the SRRs, $\gamma = R\sqrt{C/L}$, and $\omega_{LC} = 1/\sqrt{LC}$ is the inductive-capacitive (LC) resonance frequency of the SRRs.

By carefully considering the coupling coefficients and the sign in front of γ or the absence of γ (for the central SRR), similar equations can be derived for all the SRRs of the topological PTMM. This procedure results in a

modification of PTMM models employed elsewhere^{35–37}, that accounts for the configuration considered here. The equations of that model can be written in compact, matrix form as

$$\hat{\Lambda}_M \ddot{\mathbf{q}} + \hat{\Gamma} \dot{\mathbf{q}} + \mathbf{q} = \mathbf{0}, \quad (1)$$

where $\mathbf{q} = [q_1 \ q_2 \ \dots \ q_N]^T$ is an N -dimensional vector, the overdots denote differentiation over the normalized temporal variable τ , and the $N \times N$ matrices $\hat{\Lambda}_M$ and $\hat{\Gamma}$ are given by

$$\hat{\Lambda}_M = \begin{bmatrix} 1 & \lambda_M & 0 & 0 & \ddots & 0 & 0 & 0 & 0 \\ \lambda_M & 1 & \lambda'_M & \ddots & 0 & 0 & 0 & 0 & 0 \\ 0 & \lambda'_M & \ddots & \lambda_M & 0 & 0 & 0 & 0 & 0 \\ 0 & \ddots & \lambda_M & 1 & \lambda'_M & 0 & 0 & 0 & 0 \\ \ddots & 0 & 0 & \lambda'_M & 1 & \lambda'_M & 0 & 0 & \ddots \\ 0 & 0 & 0 & 0 & \lambda'_M & 1 & \lambda_M & \ddots & 0 \\ 0 & 0 & 0 & 0 & 0 & \lambda_M & \ddots & \lambda'_M & 0 \\ 0 & 0 & 0 & 0 & 0 & \ddots & \lambda'_M & 1 & \lambda_M \\ 0 & 0 & 0 & 0 & \ddots & 0 & 0 & \lambda_M & 1 \end{bmatrix}, \quad (2)$$

and

$$\hat{\Gamma} = \begin{bmatrix} +\gamma & 0 & 0 & 0 & \ddots & 0 & 0 & 0 & 0 \\ 0 & -\gamma & 0 & \ddots & 0 & 0 & 0 & 0 & 0 \\ 0 & 0 & \ddots & 0 & 0 & 0 & 0 & 0 & 0 \\ 0 & \ddots & 0 & -\gamma & 0 & 0 & 0 & 0 & 0 \\ \ddots & 0 & 0 & 0 & 0 & 0 & 0 & 0 & \ddots \\ 0 & 0 & 0 & 0 & 0 & +\gamma & 0 & \ddots & 0 \\ 0 & 0 & 0 & 0 & 0 & 0 & \ddots & 0 & 0 \\ 0 & 0 & 0 & 0 & 0 & \ddots & 0 & +\gamma & 0 \\ 0 & 0 & 0 & 0 & \ddots & 0 & 0 & 0 & -\gamma \end{bmatrix}. \quad (3)$$

Note that the two SRRs at each end of the chain interact through intra-dimer coupling λ_M , excluding thus the formation of topologically protected *edge states*. The coefficients λ_M and λ'_M can be either estimated by simple means³⁴, or calculated accurately using commercially available software packages⁴².

III. NUMERICAL SIMULATIONS

Equations (1) are integrated in time using a 4th order Runge-Kutta algorithm with a constant time-step (typically $h = 0.02$) with free-end boundary conditions, i.e., with

$$q_0(\tau) = 0, \quad q_{N+1}(\tau) = 0, \quad (4)$$

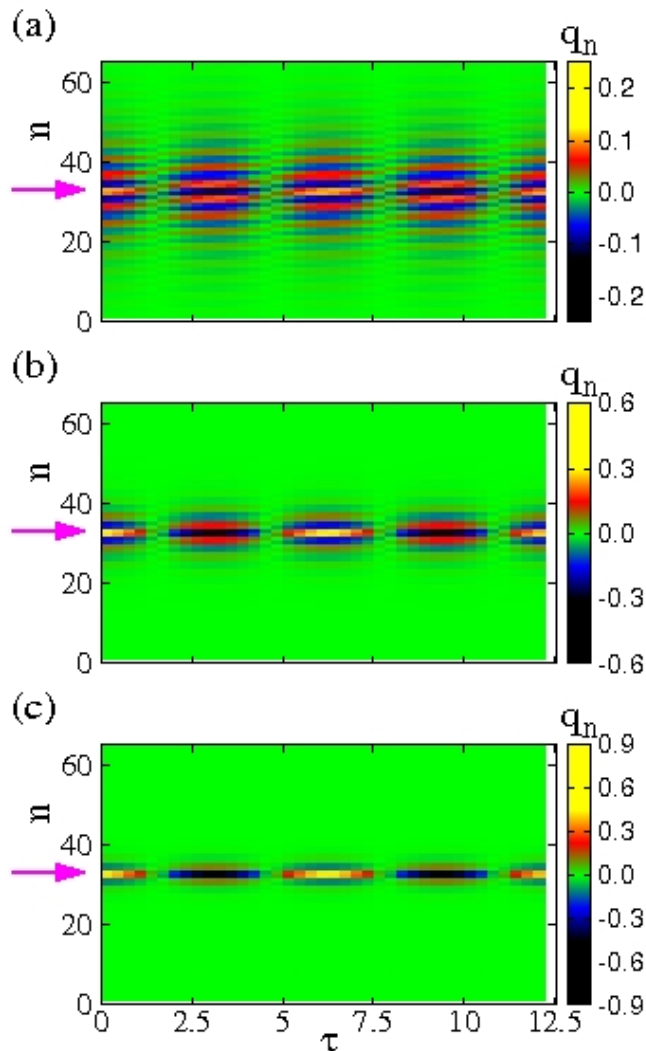


FIG. 2: (color online) Maps of the charge profiles q_n , where n is the site number ($n = 1, 2, 3, \dots, N$), as a function of normalized temporal variable τ in the topologically protected localized interface state during two oscillation periods $2T = 4\pi \simeq 12.56$, for $A = 1$, $N = 65$, $\lambda_M = -0.04$, $\gamma = 0.005$, and (a) $\lambda'_M = -0.03$ ($\delta\lambda_M = 0.01$); (b) $\lambda'_M = -0.02$ ($\delta\lambda_M = 0.02$); (c) $\lambda'_M = -0.01$ ($\delta\lambda_M = 0.03$). The (magenta) arrows indicate the position at $n = n_e = (N + 1)/2$ of the central split-ring resonator (SRR) which has neither gain nor loss.

that account for the termination of the structure in a finite system. In what follows, the system is initialized with a single-site excitation of amplitude A at the interface, i.e., with

$$q_n(\tau = 0) = A \delta_{n,n_e}, \quad \dot{q}_n(\tau = 0) = 0, \quad (5)$$

where $n_e = (N + 1)/2$ and δ_{n,n_e} is the delta function ($n = 1, \dots, N$).

In Figs. 2(a), (b), and (c), two-dimensional maps of the charge profiles q_n , where n is the site number ($n = 1, 2, 3, \dots, N$), are shown as a function of the nor-

malized temporal variable τ during two oscillation periods $2T$, where $T = 2\pi$ ($\Omega = 1$), for three dimerization strengths $\delta\lambda_M = 0.03, 0.02$, and 0.01 , respectively, and $\gamma = 0.005$. In order to obtain these profiles, the topological PTMM is initialized according to Eq. (5) with $A = 1$, and then Eqs. (1) are integrated in time for $\sim 10^5 T$ time-units (i.e., for $\sim 10^5$ periods), to eliminate transients and reach a steady state. Only the profiles obtained during the last two periods of integration are kept and mapped onto the $\tau - n$ plane in Fig. 2. These long transients originate from the fact that the initial condition is not an exact solution of the topological PTMM. Thus, some of its energy escapes away from the interface region during evolution and generates standing waves that may destroy localization. For obtaining more clear results, the SRRs with gain that belong to the dimers at the ends of the chain have been converted into lossy ones. That makes the system slightly lossy, but also helps the excessive energy to slowly dissipate and leave behind smooth profiles. These lossy ends are employed in all simulations of the dynamical equations Eqs. (1) below.

As it is observed in Fig. 2, a localized state forms at the interface (whose position at $n = n_e$ is indicated by the arrows) and moreover its localization is stronger for higher $\delta\lambda_M$. This result is independent of the amplitude A , whose only effect is to decrease the maximum of the localized states proportionally to its magnitude, since the system is linear. In earlier works on 1D configurations similar to those of Fig. 1^{13,14,39,43}, it has been argued that by interfacing two dimer chains with different topologies (i.e., the topological and the non-topological one) and thus different topological invariants, results in a topological transition accompanied by a topologically protected state at the interface such as those presented here.

In Figs. 3(a), (b), and (c), the variation of the charge profiles q_n of the topologically protected localized interface state is shown as a function of λ'_M for $\gamma = 0, 0.005$, and 0.01 , respectively. In each subfigure, the topological PTMM is initialized according to Eq. (5) with $A = 1$ for each λ'_M , and then Eqs. (1) are integrated in time for $\sim 10^5 T$ time-units for the transients to die out. The charge profiles at the end of the integration time for each λ'_M are then mapped as a function of λ'_M . Note that lossy ends, as described above, are also employed here during time-integration.

For decreasing λ'_M or equivalently decreasing $\delta\lambda_M$, the maximum of the profiles q_n at $n = n_e$ (indicated by the horizontal magenta arrows) lowers smoothly approximately at the same rate in all subfigures. At a critical $\lambda'_M = (\lambda'_M)_1$, however, the topologically protected states destabilize, leaving behind extended states which eventually vanish due to the lossy ends. With further decreasing λ'_M , in the case of $\gamma = 0.005$ and 0.01 (Figs. 3(b) and (c)), even these states destabilize at another critical $\lambda'_M = (\lambda'_M)_2$ (indicated by the vertical red arrows), where a transition from the exact to the broken \mathcal{PT} phase occurs. Obviously there is no such transition

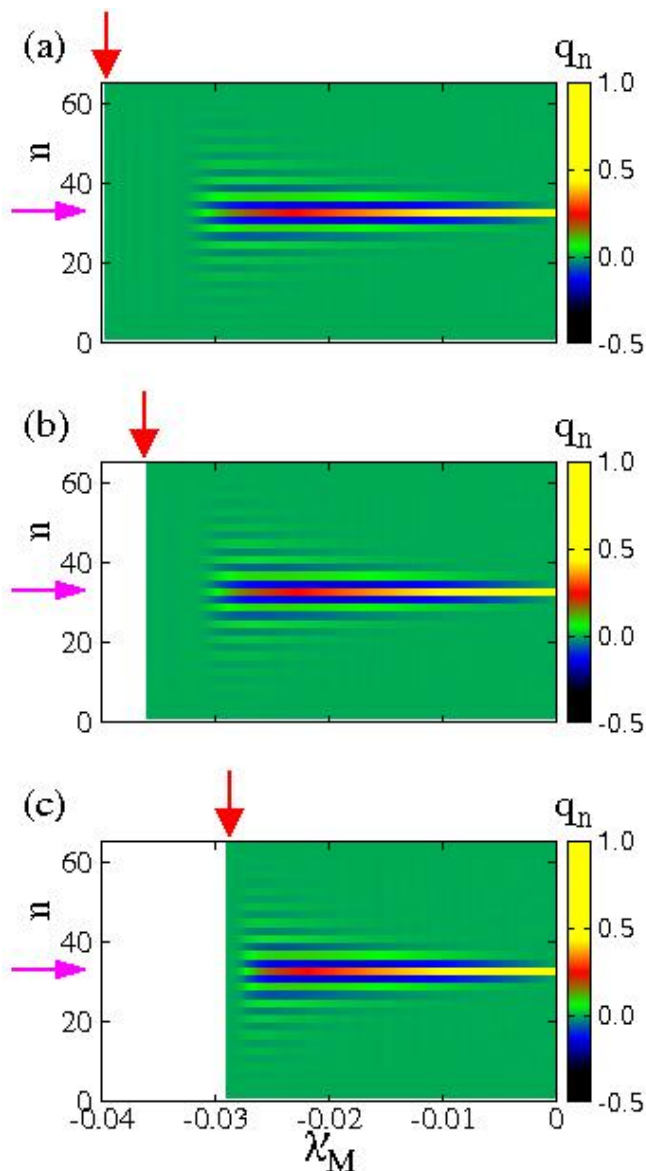


FIG. 3: (color online) Maps of the charge profiles q_n , where n is the site number ($n = 1, 2, 3, \dots, N$), as a function of the inter-dimer coupling λ'_M for $N = 65$, $\lambda_M = -0.04$, and (a) $\gamma = 0$; (b) $\gamma = 0.005$; (c) $\gamma = 0.01$. The horizontal (magenta) arrows indicate the position at $n = n_e = (N + 1)/2$ of the central split-ring resonator (SRR) which has neither gain nor loss. The vertical (red) arrows indicate the critical λ'_M that separates the exact from the broken \mathcal{PT} phase, $(\lambda'_M)_2$, whose values are -0.04 , -0.036 , and -0.029 for (a), (b), and (c), respectively.

in the case $\gamma = 0$ (Fig. 3(a)). The value of $(\lambda'_M)_1$ is -0.03275 , -0.03175 , and -0.0285 , while that of $(\lambda'_M)_2$ is -0.04 , -0.036 , and -0.029 , respectively, for $\gamma = 0$, 0.005 , and 0.01 .

At $\lambda'_M = (\lambda'_M)_1$, the topologically protected states break down due to dynamical instabilities arising independently of the existence or not of \mathcal{PT} symmetry, at least for γ relatively far from γ_c . The value of $(\lambda'_M)_2$

generally depends on $\delta\lambda_M$, and it decreases with decreasing γ . Thus, the instability at $\lambda'_M = (\lambda'_M)_2$ observed in Figs. 3(b) and (c) signifies the transition of the topological PTMM to the broken \mathcal{PT} phase where no stable states exist (the lossy ends cannot prevent this divergence). These results indicate that for the topological PTMM, the dimerization strength $\delta\lambda_M$ is the important parameter for the observation of protected topological localization. The gain-loss coefficient γ only slightly affects the profiles q_n of the protected states, as it can be inferred by comparing Fig. 3(a) with Figs. 3(b) and (c). Clearly, protected topological localization emerges even in the absence of \mathcal{PT} symmetry, i.e., for $\gamma = 0$ (Fig. 3(a)).

IV. THE QUADRATIC EIGENVALUE PROBLEM

By substituting $\mathbf{q} = \mathbf{q}_0 e^{i\Omega\tau}$ into Eq. (1) we get

$$\left\{ -\Omega^2 \hat{\Lambda}_M + i\Omega \hat{\Gamma} + \hat{\mathbf{I}}_{N \times N} \right\} \mathbf{q}_0 = \hat{\mathbf{0}}, \quad (6)$$

where $\hat{\mathbf{I}}_{N \times N}$ is the $N \times N$ identity matrix. Eq. (6) is a quadratic eigenvalue problem (QEP) that can be solved by standard eigenproblem solvers after its linearization by the classical augmentation procedure^{44,45}. In the exact \mathcal{PT} phase all the eigenfrequencies are real, and their spectrum consists of two bands separated by a gap, and an isolated mid-gap eigenfrequency equal to unity (Figs. 4 and 5). The latter corresponds to a highly localized eigenmode.

In Fig. 4, all the real eigenfrequencies are plotted as a function of λ'_M for three values of γ . For relatively high λ'_M as compared with λ_M or equivalently relatively high $\delta\lambda_M$, two distinct frequency bands are formed. The bands are separated by a gap, in which a mid-gap frequency at $\Omega = 1$ can be observed. However, for decreasing λ'_M both bands widen until they merge together at a critical value $\lambda'_M = (\lambda'_M)_2$ whose actual value depends on γ . Below that point, the until then real eigenfrequencies acquire a nonzero imaginary part that signifies the transition from the exact to the broken \mathcal{PT} phase where no stable solutions exist. In Fig. 4(a), for which $\gamma = 0$, the two bands merge at $\lambda_M = \lambda'_M$ or equivalently at $\delta\lambda_M = 0$ ($(\lambda'_M)_2 = -0.04$), while in Figs. 4(b) and (c) they merge at $\delta\lambda_M \simeq 0.00175$ ($(\lambda'_M)_2 \simeq -0.03825$) and $\simeq 0.00825$ ($(\lambda'_M)_2 \simeq -0.03175$), respectively. Note that in the presence of \mathcal{PT} symmetry ($\gamma \neq 0$), the values of $(\lambda'_M)_2$ obtained by solving the QEP are smaller than the corresponding ones obtained by solving directly the dynamical equations Eqs. (1), $(\lambda'_M)_2$, with the same set of parameters. The reason for this difference is again dynamical instabilities peculiar to \mathcal{PT} symmetric systems ($(\lambda'_M)_2 = (\lambda'_M)_2$ for $\gamma = 0$). In Fig. 4, the locations of $(\lambda'_M)_2$ are indicated by vertical red arrows, while the

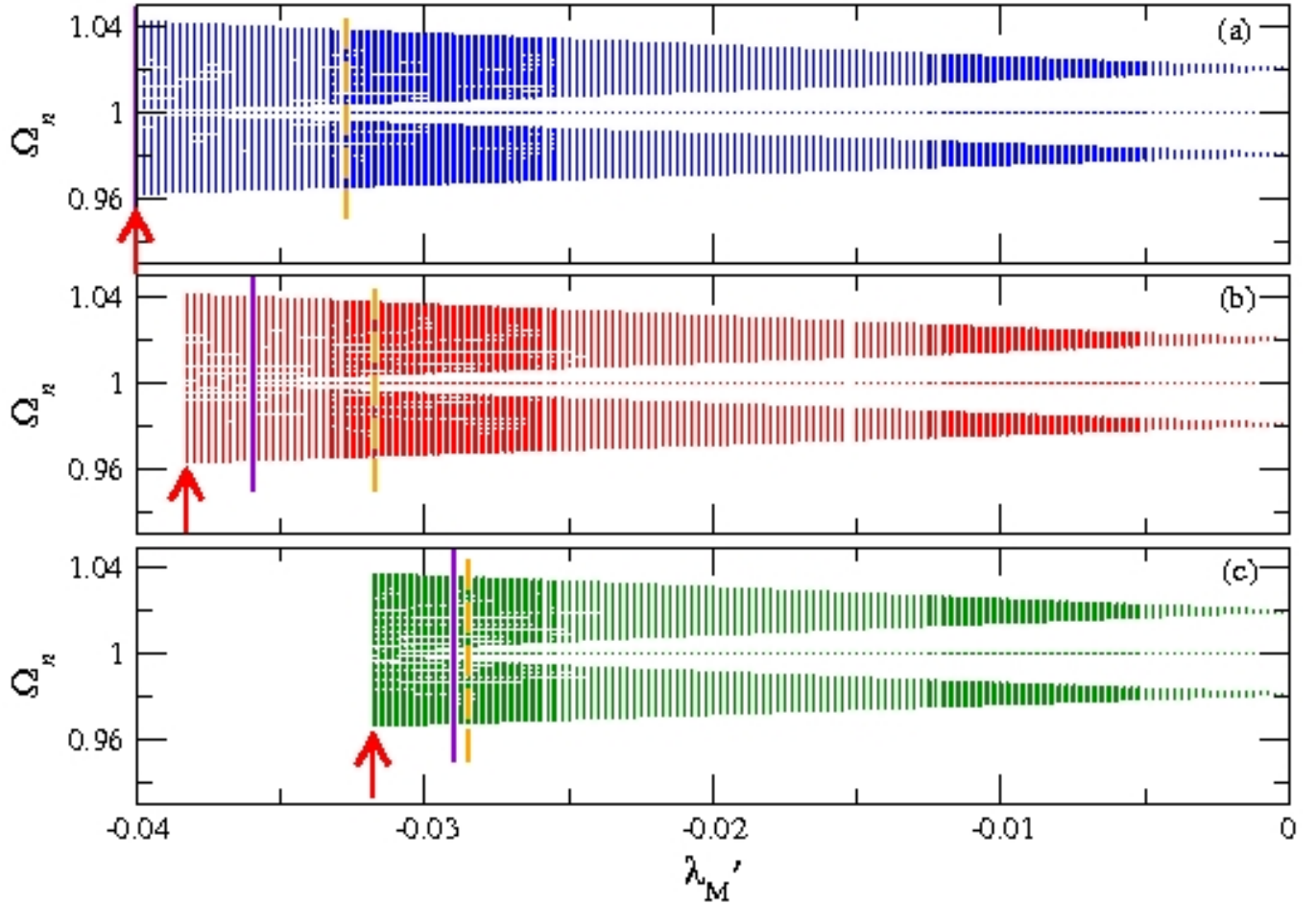


FIG. 4: (color online) Real eigenfrequencies Ω_n ($n = 1, 2, 3, \dots, N$) as a function of the inter-dimer coupling λ'_M for $N = 65$, $\lambda_M = -0.04$, and (a) $\gamma = 0$; (b) $\gamma = 0.005$; (c) $\gamma = 0.01$. The vertical (red) arrows indicate the critical λ'_M that separate real from complex eigenvalues or equivalently the exact from the broken \mathcal{PT} phase, $(\lambda'_M)_2$, whose values are $(\lambda'_M)_2 = -0.04$, -0.03825 , and -0.03175 for (a), (b), and (c), respectively. The solid-maroon and dashed-orange vertical segments indicate the values of $(\lambda'_M)_2$ and $(\lambda'_M)_1$ discussed in the context of Fig. 3.

locations of $(\lambda'_M)_1$ and $(\lambda'_M)_2$ which were defined in the context of Fig. 3 by dashed-orange and solid-maroon vertical segments, respectively.

In Fig. 5, the real eigenfrequencies of the topological PTMM are plotted as a function of γ for three values of $\delta\lambda_M$. The eigenfrequency spectrum is similar to that in Fig. 4. There are again two distinct frequency bands separated by a gap with a mid-gap eigenfrequency at $\Omega = 1$. Here, the bandwidths do not change significantly for large intervals of γ relatively far from γ_c (e.g., from $\gamma = 0$ to ~ 0.015 in Fig. 5(a)). The bandwidths are larger for lower λ'_M (lower $\delta\lambda_M$), and the two bands merge together at $\gamma = \gamma_c$ whose value depends on λ'_M .

The boundary between the exact and the broken \mathcal{PT} phase of the system is constructed numerically by solving the QEP. When all the eigenfrequencies are real, the PTMM is considered to be in the exact \mathcal{PT} phase, otherwise it is considered to be in the broken \mathcal{PT} phase. Such “ \mathcal{PT} phase diagrams” in the $\delta\lambda_M - \gamma$ plane are shown in

Fig. 6 for topological PTMMs with different N . These figures provide insights about the parameter values leading to the exact \mathcal{PT} phase. For the values of N used in Fig. 6, the parameter area providing exact \mathcal{PT} phase and thus stability and topological effects shrinks with increasing N . For larger N , however, such \mathcal{PT} phase diagrams do not change significantly with N while the boundary between the two phases approaches the line $\gamma = \delta\lambda_M$. The results of Fig. 6 can be compared to dynamic simulations for the *energetic participation number*

$$P_e = \frac{E_{tot}^2}{\sum_{n=1}^N E_n^2} \quad (7)$$

of steady states of the system on the $\delta\lambda_M - \gamma$ plane, where

$$E_n = \frac{1}{2} \{ \dot{q}_n^2 + q_n^2 + (\hat{\Lambda}_M)_{n,n+1} \dot{q}_n \dot{q}_{n+1} + (\hat{\Lambda}_M)_{n-1,n} \dot{q}_{n-1} \dot{q}_n \} \quad (8)$$

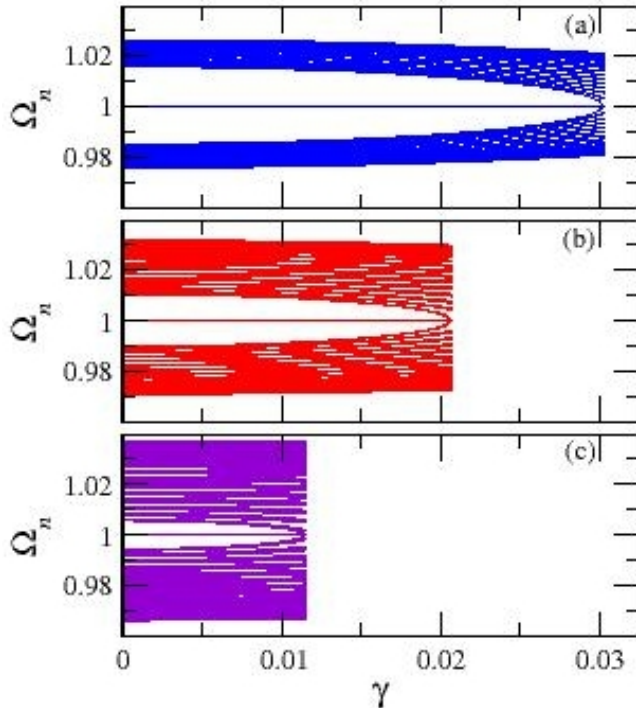


FIG. 5: (color online) Real eigenfrequencies Ω_n as a function of the gain-loss coefficient γ for $N = 65$, $\lambda_M = -0.04$, and (a) $\lambda'_M = -0.01$ ($\delta\lambda_M = 0.03$); (b) $\lambda'_M = -0.02$ ($\delta\lambda_M = 0.02$); (c) $\lambda'_M = -0.03$ ($\delta\lambda_M = 0.01$).

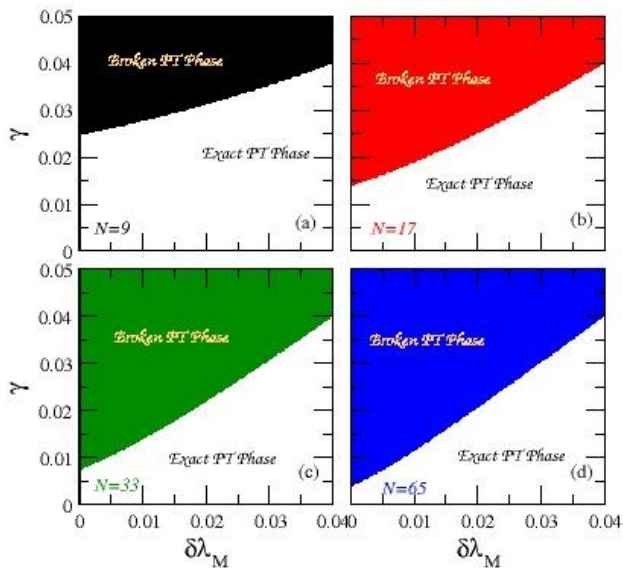


FIG. 6: (color online) \mathcal{PT} phase diagrams for topological \mathcal{PT} metamaterials with $\lambda_M = -0.04$ and (a) $N = 9$; (b) $N = 17$; (c) $N = 33$; (d) $N = 65$, on the $\delta\lambda_M - \gamma$ plane. Colored (white) areas indicate broken (exact) \mathcal{PT} phase.

and

$$E_{tot} = \frac{1}{2} \left\{ \dot{\mathbf{q}}^T \hat{\Lambda}_M \dot{\mathbf{q}} + \mathbf{q}^T \hat{\mathbf{I}}_{N \times N} \mathbf{q} \right\} \quad (9)$$

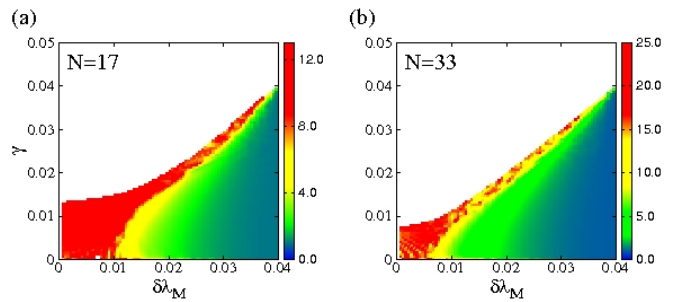


FIG. 7: (color online) The time-average of P_e over a period $T = 2\pi$, $\langle P_e \rangle_{T=2\pi}$, mapped on the $\delta\lambda_M - \gamma$ plane for $\lambda_M = -0.04$ and (a) $N = 17$; (b) $N = 33$. White areas indicate broken \mathcal{PT} phase.

are the approximate energy density and total energy, respectively, in which the terms proportional to γ are neglected. In Fig. 7, the time-average of P_e over $T = 2\pi$ (i.e., for $\Omega = 1$), $\langle P_e \rangle_{T=2\pi}$, is mapped on the $\delta\lambda_M - \gamma$ plane for $N = 17$ and 33. At each point on that plane the system is initialized with $A = 1$. The integration time is large enough to eliminate transients and lossy ends were employed. Figs. 7(a) and (b) provide a slightly lowered boundary between the exact and broken \mathcal{PT} phase compared to that in Figs. 6(b) and (c), respectively. This is due to dynamical instabilities setting in when γ approaches γ_c . Most importantly, $\langle P_e \rangle_{T=2\pi}$ quantifies the degree of localization of the topologically protected states, since it roughly measures the number of the energetically strongest excited SRRs. In a sense, it quantifies the degree of topological protection. The highest degree of localization ($\langle P_e \rangle_{T=2\pi} \sim 1 - 2$) is obtained in the blue areas, where all the energy of a state in this part of the plane is concentrated in one or two SRRs only. The degree of localization then gradually decreases in the green and yellow areas, and practically vanishes in the red areas (in the white areas, stable solutions do not exist). Note that for fixed $\delta\lambda_M$, the degree of localization decreases with increasing γ .

V. CONCLUSIONS

A topological PTMM having the configuration in Fig. 1 is considered, using equivalent circuit modeling in which the dynamics is described by a set of linear second order differential equations for the charges q_n . Direct numerical simulations demonstrate the existence of interface topologically protected localized states in the exact \mathcal{PT} phase, that oscillate with the mid-gap frequency $\Omega = 1$ of the eigenfrequency spectrum. The results presented here indicate that the *dimerization strength* $\delta\lambda_M$ is the important parameter regarding topological protection of interface localized states. Conversely, the effect of γ is much weaker as long as its value is relatively far from the critical one, γ_c ; its presence is not necessary for topo-

logical protection and even disfavors slightly localization. However, \mathcal{PT} symmetry does not destroy the topological nature of the localized interface state and thus such \mathcal{PT} -symmetric states can be realized. Given that robust topological edge states have been already observed in 1D SRR chains³², the predictions above could be experimentally confirmed at least for $\gamma = 0$.

Acknowledgements

The authors gratefully acknowledge the financial support of the Ministry of Science and Higher Education

of the Russian Federation in the framework of Increase Competitiveness Program of NUST “MISiS” (No. K2-2019-010), implemented by a governmental decree dated 16th of March 2013, N 211, and also thank the Superconducting Metamaterials Laboratory for its hospitality during visits. NL acknowledges support by the General Secretariat for Research and Technology (GSRT) and the Hellenic Foundation for Research and Innovation (HFRI) (Grant No. 203).

-
- ¹ Ling Lu, J. D. Joannopoulos, and M. Soljačić, Topological photonics, *Nat. Photon.* **8**, 821–829 (2014).
- ² Jiho Noh, Sheng Huang, K. P. Chen, and M. C. Rechtsman, Observation of Photonic Topological Valley Hall Edge States, *Phys. Rev. Lett.* **120**, 063902 (2018).
- ³ T. Ozawa, H. M. Price, A. Amo, N. Goldman, M. Hafezi, Ling Lu, M. C. Rechtsman, D. Schuster, J. Simon, O. Zilberberg, and I. Carusotto, Topological photonics, *Rev. Mod. Phys.* **91**, 015006 (2019).
- ⁴ Yu-Gui Peng, Zhi-Guo Geng, and Xue-Feng Zhu, Topologically protected bound states in one-dimensional Floquet acoustic waveguide systems, *J. Appl. Phys.* **123**, 091716 (2018).
- ⁵ D. J. Apigo, Wenting Cheng, K. F. Dobiszewski, E. Prodan, and C. Prodan, Observation of topological edge modes in a quasiperiodic acoustic waveguide, *Phys. Rev. Lett.* **122**, 095501 (2019).
- ⁶ Guancong Ma, Meng Xiao, and C. T. Chan, Topological phases in acoustic and mechanical systems, *Nat. Rev. Phys.* **1**, 281–294 (2019).
- ⁷ C. L. Kane and T. C. Lubensky, Topological boundary modes in isostatic lattices, *Nature Phys.* **10**, 39–45 (2013).
- ⁸ D. Zeb Rocklin, B. Ginge Chen, M. Falk, V. Vitelli, and T. C. Lubensky, Mechanical Weyl Modes in Topological Maxwell Lattices, *Phys. Rev. Lett.* **116**, 135503 (2016).
- ⁹ E. Prodan, K. Dobiszewski, A. Kanwal, J. Palmieri, and C. Prodan, Dynamical Majorana edge modes in a broad class of topological mechanical systems, *Nat. Comms.* **8**, 14587 (2017).
- ¹⁰ J. E. Moore, The birth of topological insulators, *Nature* **464**, 194–198 (2010).
- ¹¹ M. Z. Hasan and C. L. Kane, Colloquium: Topological insulators, *Rev. Mod. Phys.* **82**, 3045–3067 (2010).
- ¹² S. Rachel, Interacting topological insulators: A review, *Rep. Prog. Phys.* **81**, 116501 (2018).
- ¹³ S. Weimann, M. Kremer, Y. Plotnik, Y. Lumer, S. Nolte, K. G. Makris, M. Segev, M. C. Rechtsman, and A. Szameit, Topologically protected bound states in photonic parity–time-symmetric crystals, *Nature Mater.* **16**, 433–438 (2016).
- ¹⁴ H. Schomerus, Topologically protected midgap states in complex photonic lattices, *Opt. Lett.* **38**, 1912–1914 (2013).
- ¹⁵ Jianfei Yin, Massimo Ruzzene, Jihong Wen, Dianlong Yu, Li Cai, and Linfeng Yue, Band transition and topological interface modes in 1D elastic phononic crystals, *Sci. Rep.* **8**, 6806 (2018).
- ¹⁶ K. Esaki, M. Sato, K. Hasebe, and M. Kohmoto, Edge states and topological phases in non-Hermitian systems, *Phys. Rev. B* **84**, 205128 (2011).
- ¹⁷ T. E. Lee, Anomalous edge state in a non-Hermitian lattice, *Phys. Rev. Lett.* **116**, 133903 (2016).
- ¹⁸ Li-Jun Lang, You Wang, Hailong Wang, and Y. D. Chong, Effects of non-Hermiticity on Su-Schrieffer-Seeger defect states, *Phys. Rev. B* **98**, 094307 (2018).
- ¹⁹ Kenta Takata and Masaya Notomi, Photonic topological insulating phase induced solely by gain and loss, *Phys. Rev. Lett.* **121**, 213902 (2018).
- ²⁰ K. Kawabata, K. Shiozaki, M. Ueda, and M. Sato, Symmetry and topology in non-Hermitian physics, *Phys. Rev. X* **9**, 041015 (2019).
- ²¹ Xi-Wang Luo and Chuanwei Zhang, Higher-order topological corner states induced by gain and loss, *Phys. Rev. Lett.* **123**, 073601 (2019).
- ²² Do Hyeok Jeon, M. Reisner, F. Mortessagne, T. Kottos, and U. Kuhl, Non-Hermitian CT-symmetric spectral protection of nonlinear defect modes, [arXiv:2002.06570v1](https://arxiv.org/abs/2002.06570v1) (2020).
- ²³ Dan S. Borgnia, Alex Jura Kruchkov, and Robert-Jan Slager, Non-Hermitian boundary modes and topology, *Phys. Rev. Lett.* **124**, 056802 (2020).
- ²⁴ Tun Cao and Shuai Wang, Topological insulator metamaterials with tunable negative refractive index in the optical region, *Nanoscale Res. Lett.* **8**, 526 (2013).
- ²⁵ Y. Barlas and E. Prodan, Topological braiding of non-Abelian midgap defects in classical metamaterials, *Phys. Rev. Lett.* **124**, 146801 (2020).
- ²⁶ H. N. S. Krishnamoorthy, Z. Jacob, E. Narimanov, I. Kretzschmar, and V. M. Menon, Topological transitions in metamaterials, *Science* **336**, 205–209 (2012).
- ²⁷ Changxu Liu, Wenlong Gao, Biao Yang, and Shuang Zhang, Disorder-induced topological state transition in photonic metamaterials, *Phys. Rev. Lett.* **119**, 183901 (2017).
- ²⁸ A. S. Meeussen, E. C. Oğuz, Y. Shokef, and M. van Hecke, Topological defects produce exotic mechanics in complex metamaterials, *Nature Phys.* **16**, 307–311 (2020).
- ²⁹ V. K. Kozin, I. A. Shelykh, A. V. Nalitov, and I. V. Iorsh, Topological metamaterials based on polariton rings, *Phys. Rev. B* **98**, 125115 (2018).

- ³⁰ T. Kotwal, H. Ronellenfitsch, F. Moseley, A. Stegmaier, R. Thomale, and J. Dunkel, Active topoelectrical circuits, arXiv:1903.10130 (2019).
- ³¹ H. U. Voss and D. J. Ballon, Topological modes in radiofrequency resonator arrays, *Phys. Lett. A* **384**, 126177 (2020).
- ³² Jun Jiang, Zhiwei Guo, Yaqiong Ding, Yong Sun, Yunhui Li, Haitao Jiang, and Hong Chen, Experimental demonstration of the robust edge states in a split-ring-resonator chain, *Opt. Express* **26**, 12891 (2018).
- ³³ Jun Jiang, Jie Ren, Zhiwei Guo, Weiwei Zhu, Yang Long, Haitao Jiang, and Hong Chen, Seeing topological winding number and band inversion in photonic dimer chain of split-ring resonators, *Phys. Rev. B* **101**, 165427 (2020).
- ³⁴ N. Lazarides, M. Eleftheriou, and G. P. Tsironis, Discrete breathers in nonlinear magnetic metamaterials, *Phys. Rev. Lett.* **97**, 157406 (2006).
- ³⁵ N. Lazarides and G. P. Tsironis, Gain-driven discrete breathers in PT-symmetric nonlinear metamaterials, *Phys. Rev. Lett.* **110**, 053901 (2013).
- ³⁶ G. P. Tsironis and N. Lazarides, PT-symmetric nonlinear metamaterials and zero-dimensional systems, *Appl. Phys. A* **115**, 449-458 (2014).
- ³⁷ N. Lazarides and G. P. Tsironis, Compact localized states in engineered flat-band PT metamaterials, *Sci. Rep.* **9**, 4904 (2019).
- ³⁸ Jung-Wan Ryu, Nojoon Myoung, Sungjong Woo, Ara Go, Sang-Jun Choi, and Hee Chul Park, Emergent localized states at the interface of a twofold PT-symmetric lattice, arXiv:1904.00444v1 (2019).
- ³⁹ C. Poli, M. Bellec, U. Kuhl, F. Mortessagne, and H. Schomerus, Selective enhancement of topologically induced interface states in a dielectric resonator chain, *Nat. Comms.* **6**, 6710 (2015).
- ⁴⁰ L. Jin, P. Wang, and Z. Song, Su-Schrieffer-Seeger chain with one pair of PT-symmetric defects, *Sci. Rep.* **7**, 5903 (2017).
- ⁴¹ L. Jin, Topological phases and edge states in a non-Hermitian trimerized optical lattice, *Phys. Rev. A* **96**, 032103 (2017).
- ⁴² N. N. Rosanov, N. V. Vysotina, A. N. Shatsev, I. V. Shadrivov, D. A. Powell, and Yu. S. Kivshar, Discrete dissipative localized modes in nonlinear magnetic metamaterials, *Opt. Express* **19**, 26500 (2011).
- ⁴³ A. Blanco-Redondo, I. Andonegui, M. J. Collins, G. Harari, Y. Lumer, M. C. Rechtsman, B. J. Eggleton, and M. Segev, Topological optical waveguiding in silicon and the transition between topological and trivial defect states, *Phys. Rev. Lett.* **116**, 163901 (2016).
- ⁴⁴ W. J. Duncan and A. R. Collar, Matrices applied to the motions of damped systems, *Phil. Mag.* **19**, 197-219 (1935).
- ⁴⁵ D. Afolabi, Linearization of the quadratic eigenvalue problem, *Computers & Structures* **26**, 1039-1040 (1987).